

Parametric Study of Hypersonic Boundary Layer Flow over Discrete Surface Roughness Using a Hybrid DSMC/Navier-Stokes Solver

Journal:	<i>2011 Hawaii Summer Conferences</i>
Manuscript ID:	Draft
IuMeetingID:	2220
Date Submitted by the Author:	n/a
Contact Author:	Stephani, Kelly; The University of Texas at Austin, Aerospace Engineering

SCHOLARONE™
Manuscripts

Parametric Study of Hypersonic Boundary Layer Flow over Discrete Surface Roughness Using a Hybrid DSMC/Navier-Stokes Solver

K. A. Stephani* D. B. Goldstein† and P. L. Varghese‡

Department of Aerospace Engineering, The University of Texas at Austin

The effects of rarefaction on hypersonic boundary layer flow over various discrete surface roughness configurations are examined parametrically for $M_\infty = 3.0$ flow over a flat plate. The roughness heights are chosen such that the local Knudsen number ($Kn = \lambda/k$) in the region of the roughness are $O(10^{-2})$, where k is the height of the protuberance and λ is the molecular mean free path. In this regime, the continuum approximations of zero velocity and no thermal slip at the wall begin to break down, and thermal non-equilibrium effects may become more prominent due to a relative increase in time required for thermal equilibration. The aim of this work is to address the significance of rarefaction effects in modeling the disturbance field generated by hypersonic boundary layer flow over surface roughness using a hybrid of the DAC and DPLR numerical simulation codes. Parametric studies have been conducted to examine flow over a flat plate with a smooth, oblique fence-like roughness for a $M_\infty = 3.0$ five-species air flow over a flat plate. The radius of curvature at the top of the roughness is varied to examine the influence of this parameter on the flowfield and distributed surface quantities. Hybrid DAC solutions are generated and compared to the DPLR solutions generated with slip and no-slip wall conditions. The vibrational non-equilibrium observed in the shock, expansion and shear layer regions surrounding the roughness is found to impact the pressure at the surface, and the DPLR slip model predicts higher velocity slip near the expansion region at the surface of the roughness. The total heat flux on the surface of the protuberance is also examined. It is found that the hybrid DAC solution predicts a heating augmentation to the roughness that is 20 – 30% below the DPLR slip wall solution, and 30 – 50% below the DPLR no-slip wall solution for the roughness configurations examined.

Nomenclature

Kn	= λ/L Knudsen number based on specified characteristic length L
M_∞	= freestream Mach number
M_e	= boundary layer edge Mach number
T_{tr}, T_r, T_{vib}	= translational, rotational and vibrational temperature
k	= roughness height [m]
p	= pressure [Pa]
f_s	= non-equilibrium surface velocity distribution function
$f_{S,max}$	= Maxwellian velocity distribution function
Γ_s	= non-equilibrium surface perturbation function

*Ph.D. candidate, Department of Aerospace Engineering, The University of Texas at Austin, 210 E 24th Street, Austin, TX 78712, e-mail: kelly.stephani@mail.utexas.edu

†Professor, Department of Aerospace Engineering, The University of Texas at Austin, 210 E 24th Street, Austin, TX 78712, e-mail: david@cfdlab.ae.utexas.edu

‡Professor and Department Chair, Department of Aerospace Engineering, The University of Texas at Austin, 210 E 24th Street, Austin, TX 78712 e-mail: varghese@mail.utexas.edu

k_b	= Boltzmann constant
Q_{CE}	= macroscopic quantities for hybrid interface boundary condition
$Z_r, Z_{vib}^{NS}, Z_{vib}^{DSMC}$	= rotational collision number and vibrational collision number (for DSMC or Navier-Stokes)
δ_T	= thermal boundary layer thickness
τ_v^{Park}	= Park's high-temperature correction for vibrational relaxation time
τ_v^{MW}	= Millikan and White vibrational relaxation time correlation
ξ_v	= vibrational degrees of freedom for harmonic oscillator
θ_v	= characteristic vibrational temperature
ν_s	= collision frequency of species s
n	= number density [m^{-3}]
u, v, w	= streamwise, spanwise and wall-normal bulk velocity [m/s]
C_x, C_y, C_z	= surface-normal (x) and tangential (y, z) thermal velocity components
x, y, z	= streamwise, spanwise and wall-normal spatial coordinates [m]
χ_s	= molar fraction of species $s = N_2, O_2, NO, N, O$
λ_{HS}	= $(1/\sqrt{2}\pi n d^2)$ molecular mean-free-path based on hard sphere model [m]
T_w	= wall temperature [K]
γ_w	= catalytic efficiency
a_c	= accommodation coefficient
d_{ref}	= variable hard sphere (VHS) reference diameter [\AA]
T_{ref}	= VHS reference temperature [K]
ω	= VHS temperature exponent
$\sigma_{T,ref}$	= VHS reference cross section
g_{ref}	= VHS reference relative thermal speed
$\Omega_s^2(2), \Omega_{st}^1(1), \Omega_{st}^2(2)$	= collision integrals for species s, t
m^*	= $\left(\frac{m_s m_t}{m_s + m_t}\right)$ reduced mass of s, t collision pair
β	= $\sqrt{\frac{m}{2kT}}$ inverse of most probable thermal speed [m^{-1}]
q_i	= heat flux vector
τ_{ij}	= shear stress tensor
r_1, r_2	= radii of curvature describing roughness geometry
l	= length of roughness geometry
x_c	= streamwise location of roughness center on a flat plate
q_o	= wall heating on a flat plate at the location x_c [W/m^2]
q_w	= local surface heat flux [W/m^2]
V_{slip}	= surface slip velocity x_c

subscripts

∞	= freestream condition
e	= boundary layer edge condition
w	= wall condition
kk	= flow conditions at the height of roughness k
NEQ	= thermal non-equilibrium

I. Introduction

The transition of boundary layer flow from a laminar to turbulent state has been the subject of study for many years. Predicting boundary layer transition is an important component of hypersonic vehicle design, as transition to turbulence can significantly alter the aerodynamic loads on the vehicle as well as cause a substantial increase in aerodynamic heating. In optimizing the design of a reentry vehicle thermal protection system, it is desirable to determine the altitude at which transition is expected to occur as well as the transition location along the body. This is a very complex problem, as there are many factors thought to affect transition location, including the boundary layer edge Mach number, crossflow, wall temperature, roughness, disturbances introduced from the freestream and structural vibrations.¹ Recent progress has been made toward developing an understanding of the physical mechanisms responsible for roughness-induced boundary layer transition² but there remain many difficulties in understanding the complete transition process for either incompressible or compressible flow regimes.³

A recent flight experiment was carried out as part of the STS-119 mission to address this issue.⁴ In the experiment, a fixed-height boundary layer trip was integrated into a tile on the Orbiter located midway between the main gear door and the wing leading edge (Figure 1). Tiles instrumented with pressure sensors and thermocouples were used to gather transition onset data near the roughness and in the wake downstream, including one thermocouple positioned on the trip itself. Additionally, infrared images highlighting boundary layer transition on the Orbiter's belly were gathered by a Navy P-3 Orion aircraft during a portion of the re-entry trajectory. The freestream Mach number was approximately 15 at the onset of transition induced by the trip, and the roughness height k was approximately one quarter of the thickness of the approaching boundary layer. Based on these conditions, initial estimates indicate that Kn was of $O(10^{-2} - 10^{-3})$ in the region of the roughness, which, in terms of the trip height used in this experiment, implies that k is $O(10^2 \lambda - 10^3 \lambda)$.

In this transitional Knudsen number regime, it is expected that the continuum assumption of no-slip at the wall begins to break down, and regions of thermal non-equilibrium may become more pronounced due to the increase in time required for equilibration of the flow compared to flow times.⁵ That Kn_k is of $O(10^{-2})$ may have significant consequences on the development of the detailed flowfield in the region of the surface roughness. Both experiments^{3,6} and numerical simulations⁷⁻⁹ have revealed the formation and interaction of a variety of flow structures around simple, discrete roughness elements in boundary layer flow, including a horseshoe vortex system developing in front of the roughness which extends downstream into the wake region, and a shear layer generated at the top surface of the roughness. In addition, regions of recirculating flow may form upstream and downstream of the roughness element, generating shocks and expansions. Rarefaction effects result in thermal and velocity slip at the surface of the roughness, which would modify the details of the flowfield by which the disturbance field (i.e., the shear layer and horseshoe vortex system, etc.) develops downstream. This may ultimately have an impact on the instabilities introduced by the roughness into the boundary layer flow, and most importantly, on the transition location itself.

To accurately capture the influence of rarefaction in these types of problems, a hybrid solution¹⁰⁻¹² is formed in the region of the boundary layer trip using DAC (DSMC Analysis Code)¹³ and DPLR (Data Parallel Line Relaxation method for the Navier-Stokes equations).¹⁴ The flowfields considered in this work examine boundary layer flow over a discrete roughness geometry on a flat plate. While the flowfield conditions examined in this work are restricted to high altitudes cases, which lie outside of the regime in which roughness-induced transition is expected, this work aims to address the influence of rarefaction on the details of the complex flowfield generated by the boundary layer flow over the roughness. The mean flow over the flat plate geometry considered herein is certainly within the continuum limit and can be accurately modeled using DPLR. The details of the Navier-Stokes simulation are provided in the next section (Section II(A)). The macroscopic properties obtained from the DPLR solution are then used to generate the hybrid interface boundary condition for DAC, which is in turn used to model the detailed flow in the region of the roughness. Discussion of the hybridization approach and the details of the hybrid DAC/DPLR simulation and the method used for matching transport properties between the two solvers may be found in Stephani *et al.*⁷ Results from the hybrid simulation are presented in Section III along with the corresponding flowfield solution obtained from DPLR for comparison, and concluding remarks are provided in Section IV.

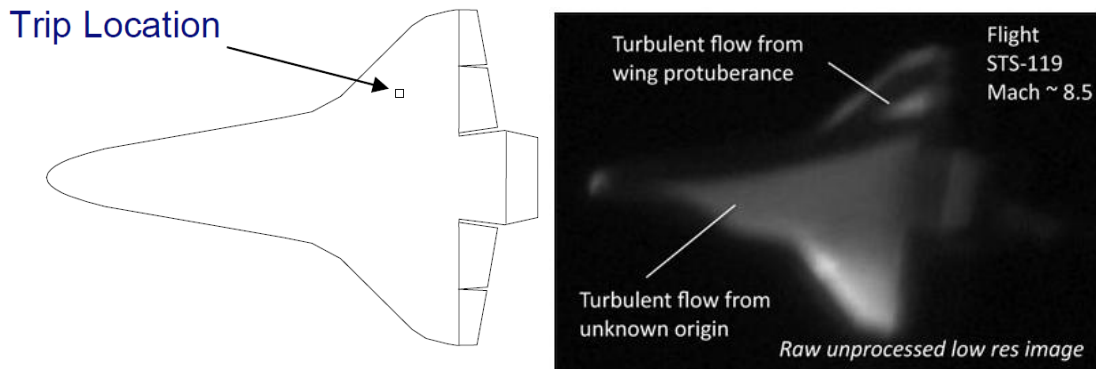


Figure 1. Schematic of boundary layer trip location on Orbiter and corresponding infrared image. (left) Fixed height boundary layer trip positioned midway between the wing leading edge and the main gear door.⁴ (right) Infrared image captured by Navy P-3 Orion aircraft during re-entry of Orbiter. Wedge of turbulent heating is seen downstream of boundary layer trip.¹⁵

II. Hybrid Approach Using DAC and DPLR

To examine the effects of rarefaction on this problem, solutions are obtained using a hybrid of two codes, DAC and DPLR. DAC uses the direct simulation Monte Carlo (DSMC) method to simulate rarefied gas environments, and was developed at NASA-JSC. The DSMC method is a particle-based approach which simulates flow at the molecular level using statistically representative particles since simulating each molecule is computationally prohibitive. Each simulated particle has a specific position, velocity and internal energy, and intermolecular collisions are treated on a probabilistic basis. Macroscopic quantities of the flow field may be evaluated by taking averages over the microscopic properties of simulated particles. The DSMC method is an attractive way to simulate rarefied flows because it inherently captures thermal and velocity slip with a variety of gas-wall interaction models. Since the DSMC method is a particle-based approach, it does become expensive to model near-continuum flows, especially over large domains. DPLR (originally developed by Wright, Candler and Bose and further developed at NASA-Ames) uses the Data Parallel Line Relaxation method to solve the Navier-Stokes equations and is used to solve high-fidelity re-entry flow problems. Although DPLR is intended for simulations of viscous flows in the continuum regime, it does have a Maxwellian slip model for implementing velocity and temperature slip at the wall. Both codes are capable of performing either serial or fully parallel computations for two-dimensional, axi-symmetric or three-dimensional flowfields.

A. Navier-Stokes Flowfield Solution (DPLR)

The DPLR code was used to generate the flowfield solution over a flat plate with an edge Mach number of $M_e = 2.96$. In this work, all flowfields generated with DPLR were solved with implicit time integration as steady-state solutions. A third-order upwind-biased MUSCL Steger-Warming scheme with a minmod flux limiter is used for the extrapolation of the Euler fluxes in the streamwise, wall-normal and spanwise directions. The eigenvalue limiter values were chosen to minimize additional dissipation within the boundary layer.

The boundary layer edge conditions pertaining to the cases presented here are outlined in Table 1. The roughness height considered in this study is $k = 0.0875m$, which is one-quarter of the thermal boundary layer thickness δ_T . These cases were modeled using a five-species air mixture (N_2, O_2, NO, N, O) model assuming frozen chemistry. Both rotational and vibrational thermal nonequilibrium are considered in these cases. Species mass diffusion fluxes were approximated using the self-consistent effective binary diffusion (SCEBD) model, and the Yos approximate mixing rule model was employed to determine the mixture viscosity and thermal conductivity coefficients.

The detailed flowfield solution in the region of the roughness was generated in two steps. First, a two-dimensional flat-plate boundary layer solution was obtained, and the appropriate roughness location along the plate was determined such that $k/\delta_T = 0.25$ as discussed above. The boundary layer flowfield quantities

were then extracted from the flat-plate solution to serve as the inflow boundary condition to a smaller, more detailed three-dimensional solution near the roughness. The roughness geometry and associated parameters considered in this work are described in detail in Section III. Both slip and no-slip isothermal boundary conditions were imposed at the solid surface in order to examine the effects of thermal and velocity slip on the heating to the roughness as well as on the flow structures generated near the roughness and in the wake. The isothermal wall temperature prescribed in these cases corresponds to the radiative equilibrium wall temperature at the location of the roughness in an undisturbed boundary layer flow, with a constant emissivity, $\epsilon = 0.8$.

Table 1. Boundary layer edge conditions at trip location

M_∞	3.0
u_∞	4214m/s
T_∞	4000K
p_∞	71.8Pa
ρ_∞	$5.0 \times 10^{-5} \text{ kg/m}^3$
λ_∞	$1.924 \times 10^{-3} \text{ m}$
M_e	2.96
u_e	4177m/s
T_e	4032K
ρ_e	$5.05 \times 10^{-5} \text{ kg/m}^3$
λ_e	$1.905 \times 10^{-3} \text{ m}$

B. Hybrid Flowfield Solution (DAC)

After obtaining the DPLR solution, the flowfield properties in the near-field region of the boundary layer trip are used to generate the boundary conditions required for the detailed hybrid solution. The hybrid interface is formed by first extracting macroscopic quantities generated from the Navier-Stokes solution in a plane of data that is coincident with the hybrid interface plane. DSMC simulations require an initialization of the particle thermal velocities; this is generally achieved by utilizing either a volume reservoir or surface reservoir approach.¹⁶ In this work we employ a nonequilibrium surface reservoir approach for particle generation within a boundary layer.¹⁷ The particles are generated from a nonequilibrium surface distribution specified by:

$$f_S = f_{S,MAX} \Gamma_S \quad (1)$$

Here we have $f_{S,MAX}$ defined as:

$$f_{S,MAX} = \frac{1}{2\pi} \left(\frac{m}{kT} \right)^2 (C_x + u) \exp \left[-\frac{m}{2kT} (C_x^2 + C_y^2 + C_z^2) \right] \quad (2)$$

and Γ_S is defined as:

$$\begin{aligned} \Gamma_S = & \frac{\Gamma / (u\sqrt{\pi}\beta)}{\left[1 + \operatorname{erf}(\beta u) + \frac{1}{u\sqrt{\pi}\beta} \exp(-\beta^2 u^2) - \frac{2}{5\sqrt{\pi}} \beta \frac{q_x}{nk_b T} \exp(-\beta^2 u^2) \right]} \\ & - \left[\frac{1}{u\sqrt{\pi}\beta} \exp(-\beta^2 u^2) + \frac{1}{2} [1 + \operatorname{erf}(\beta u)] \right] \frac{\tau_{xx}}{nk_b T_{tr}} \\ & - \frac{1}{2} \left[\frac{1}{u\sqrt{\pi}\beta} \exp(-\beta^2 u^2) + [1 + \operatorname{erf}(\beta u)] \right] \frac{\tau_{yy}}{nk_b T_{tr}} \\ & - \frac{1}{2} \left[\frac{1}{u\sqrt{\pi}\beta} \exp(-\beta^2 u^2) + [1 + \operatorname{erf}(\beta u)] \right] \frac{\tau_{zz}}{nk_b T_{tr}} \end{aligned} \quad (3)$$

The surface reservoir approach may be thought of as a surface that emits randomly distributed particles at a rate that is consistent with the fluid density and temperature. To generate particles from this non-equilibrium distribution, we follow an acceptance-rejection algorithm very similar to the approach outlined

in Garcia & Alder.¹⁸ The macroscopic quantities Q_{CE} required for generating the DSMC particles at the non-equilibrium hybrid interface are thus:

$$Q_{CE} = \left(n \ T \ \vec{V} \ \chi_s \ P \ \tau_{ij} \ q_i \right) \quad (4)$$

C. Consistent Treatment of the Transport Properties and Vibrational Relaxation

The details of the transport of mass, momentum and energy as well as the rotational and vibrational thermal relaxation are handled differently by the DAC and DPLR solvers. DPLR uses various models to determine the mass diffusion coefficient and viscosity and thermal conductivity coefficients. For this work, the viscosity and thermal conductivity coefficients are determined from Yos approximate mixing rules. The transport properties within the Yos model are determined from expressions involving the collision integrals, $\Omega_{st}^1(1)$ and $\Omega_{st}^2(2)$, and a curve-fit is employed to obtain these collision integrals as a function of temperature.¹⁹ DAC does not use a direct model to obtain the transport properties; rather, DAC uses a variable hard sphere (VHS) model in which the simulation particles are modeled as hard spheres of diameter d which is a function of g , the relative speed of the collision pair. The transport properties are a result of the transfer of mass, momentum and energy through particle movement and collision dynamics,²⁰ and the transport properties are thus adjusted by tuning the parameters used in the collision model. It is possible, however to compute the collision integrals $\Omega_{st}^1(1)$ and $\Omega_{st}^2(2)$ in terms of the VHS parameters in DAC, thereby allowing for the VHS parameters to be used to ‘tune’ the DAC solver in order to achieve consistency between the DAC and DPLR transport properties. The details of this process may be found in Stephani *et al.*¹⁷ The resulting fitted VHS parameters employed in this work are listed in Table 2, and the corresponding transport coefficients are plotted as a function of temperature in Figures 2 and 3.

Table 2. 5-Species Air VHS Parameters

	$d_{ref}[\text{\AA}]$	$T_{ref}[K]$	ω
N_2	2.8296	2880	0.68
O_2	3.8875	2880	0.68
NO	3.1760	2880	0.68
N	2.4206	2880	0.72
O	2.297	2880	0.6801

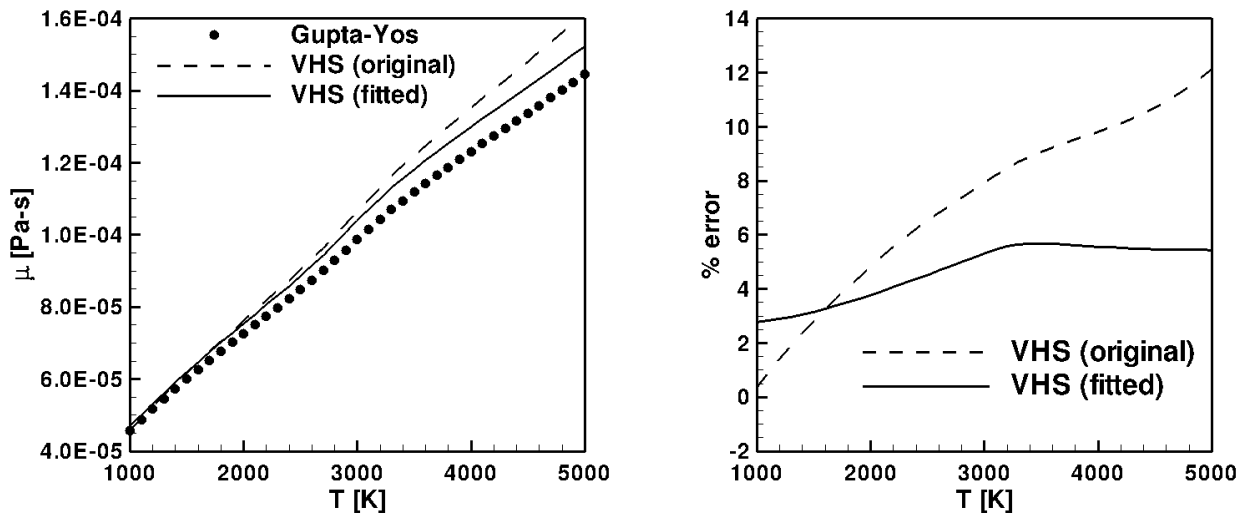


Figure 2. Gupta-Yos and VHS 5-species air mixture viscosity as a function of temperature (left) and percent error of VHS mixture viscosity to Gupta-Yos model (right)

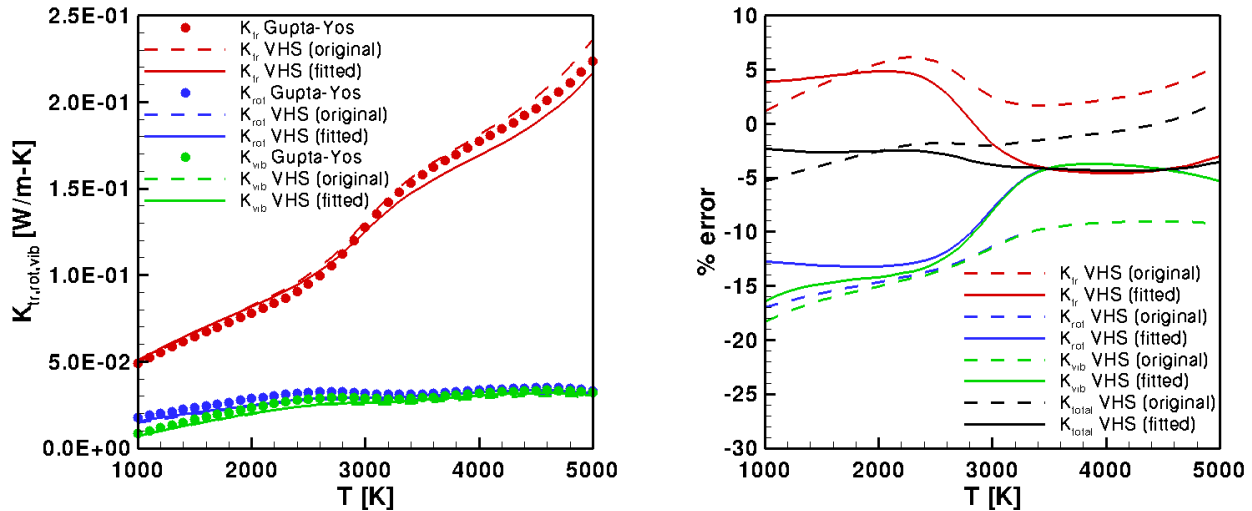


Figure 3. Gupta-Yos and VHS 5-species air mixture translational, rotational and vibrational conductivities as a function of temperature (left) and percent error of VHS thermal conductivities to Gupta-Yos model (right). Errors are expressed for each mode (translation, rotation and vibration) as well as a total error relative to the Gupta-Yos value.

Vibrational relaxation times in both DPLR and DAC are determined using the Landau-Teller model for simple harmonic oscillators, along with empirical correlations of the vibrational relaxation times from Millikan and White and Park's high-temperature correction.^{21,22} DSMC uses the Larsen-Borgnakke method for redistribution of energy among the modes, with the probability of an inelastic collision determined as $1/Z$, where Z is the collision number of the internal mode. The rotational collision number used in the present work is assumed to be constant, with $Z_r = 5$. To ensure consistency in the vibrational relaxation times achieved in both solvers, the DSMC vibrational collision number is determined according to the expression:²³

$$Z_v^{DSMC} = Z_v^{NS} \left(\frac{1}{1 + \frac{0.5\xi_v^2 \exp(\theta_v/T)}{(4-2\omega)}} \right) \quad (5)$$

where θ_v is the characteristic vibrational temperature and ξ_v is the temperature-dependent number of vibrational degrees of freedom for a harmonic oscillator given by:

$$\xi_v = \left(\frac{2\theta_v/T}{\exp(\theta_v/T) - 1} \right) \quad (6)$$

The Navier-Stokes collision number, Z_v^{NS} is computed as:

$$Z_v^{NS} = (\tau_v^{MW} + \tau_v^{Park})\nu \quad (7)$$

where τ_v^{Park} is the high-temperature correction due to Park:²²

$$\tau_v^{Park} = \frac{1}{n \sqrt{\frac{8k_b T}{\pi m}} \sigma} \quad (8)$$

and τ_v^{MW} is determined from the empirical correlation:²¹

$$\tau_v^{MW} = \frac{1}{p} \exp(A(T^{-1/3} - B) - 18.42) \quad (9)$$

In (9), A and B are vibrational constants for each collision pair,²² and p is in atmospheres. The collision frequency ν of species s in a mixture is determined by:

$$\nu_s = \sum_t \left(n_t (d_{ref})_t^2 \left(\frac{8\pi k_b T_{ref,t}}{m_t^*} \right)^{1/2} \left(\frac{T}{T_{ref,t}} \right)^{1-\omega_t} \right) \quad (10)$$

All quantities in (5) are determined according to the DSMC cell-based macroscopic quantities as outlined in Deschenes *et al.*²⁴ This vibrational relaxation approach has been demonstrated to improve agreement between the vibrational relaxation times produced by DSMC and continuum flow solvers in a heat bath of five species air.²⁵ In the current work, this relaxation method is applied to examine the vibrational relaxation of a five species air mixture within a hypersonic boundary layer.

III. Results

A. Roughness Configurations and Parameters

The general roughness geometry considered in this parametric study is an elongated hump on a flat plate. In every case presented, the roughness is oriented at an angle of 45° with respect to the oncoming flow, and the roughness height ($k = 8.75\text{cm}$) is one-quarter of the thermal boundary layer thickness of an undisturbed boundary layer profile. The Reynolds numbers relevant to this problem are listed in Table 3 and are defined as follows:

$$Re_{x_c} = \frac{\rho_e u_e x_c}{\mu_e} \quad (11)$$

where the flow quantities are taken as the undisturbed thermal boundary layer edge values at a distance x_c downstream from the leading edge of the flat plate, and x_c is the center of the roughness.

$$Re_{\delta_T} = \frac{\rho_e u_e \delta_T}{\mu_e} \quad (12)$$

where δ_T is the thermal boundary layer thickness at the roughness center x_c .

$$Re_{kk} = \frac{\rho_k u_k k}{\mu_k} \quad (13)$$

where the flow quantities are taken as the values at the height of the roughness k in an undisturbed boundary layer flow at the roughness center x_c . While this geometry allows for the variation of many parameters, (e.g., height, length, orientation with respect to the flow, steepness of hump, etc.), this study focuses on the variation of the radius of curvature r_1 . Two cases are examined; the first roughness (Figure 4, left) has a radius of curvature $r_1 = 20.0\text{mm}$. This radius of curvature is approximately 12 times the molecular mean free path at the height of the roughness in an *undisturbed boundary layer*, λ_k (Table 3). The actual mean free path at the height of the roughness is smaller as the flow is first processed by a weak oblique shock induced by the roughness. The second roughness (Figure 4, right) has a radius of curvature $r_1 = 2.0\text{mm}$, which is 1.25 times the molecular mean free path at height k in an undisturbed boundary layer. The radius of curvature at the wall, r_2 , is 50-100 times larger than the molecular mean free path at the wall in an undisturbed boundary layer (λ_w) in both cases examined. The mean free path varies over the height of the roughness due to the variation of properties in the boundary layer, but the roughness height is $O(10^1 - 10^2)$ mean free paths. The steepness of the hump, which is related to the ratio r_1/r_2 , is held fixed, as well as the roughness height, k and roughness length, $l = 8k$ (Figure 5).

B. Navier-Stokes and Hybrid DSMC Solutions – Case 1: $r_1 = 20.0\text{mm}$

In all cases presented, the roughness center x_c is located 10.45m downstream from the flat plate leading edge. The DPLR solution is solved on a domain with dimensions $(x, y, z) = (80k, 10k, 30k)$ using approximately 7×10^6 grid points, and the roughness center is located at the spanwise center of the domain at a location $35k$ from the front of the domain. Figure 6 (top) shows the DPLR surface and flowfield mesh on and around the roughness for the $r_1 = 20.0\text{mm}$ and $r_1 = 2.00\text{mm}$ geometries. The inflow boundary conditions (specified at the x_{min} and y_{max} boundaries) are prescribed from the corresponding 2-D flat plate boundary layer solution without the roughness, the outflow boundary condition (at the x_{max} boundary) is specified as supersonic outflow, and the side walls are treated as periodic boundaries. The hybrid solution is solved on a

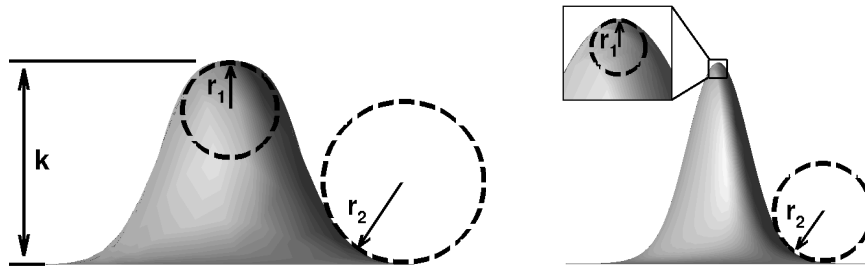


Figure 4. Profiles of discrete roughness geometries examined in parametric study. Two values of the radius r_1 are considered; $r_1 = 20.0\text{mm}$ (left) and $r_1 = 2.0\text{mm}$ (right), with the ratio between r_1 and r_2 held fixed. The roughness height and length remain constant.

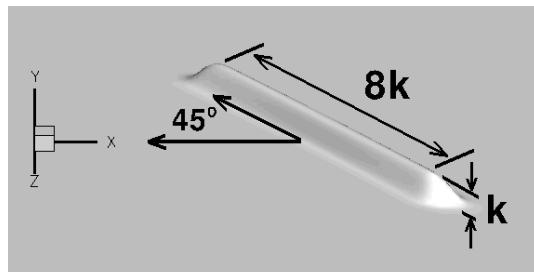


Figure 5. Perspective view of the discrete roughness shown in Figure 4. The roughness is oriented at an angle of 45° with respect to the oncoming boundary layer flow.

smaller domain surrounding the roughness, with dimensions $(x, y, z) = (20k, 3k, 13k)$. The roughness center is located at the spanwise center of the domain at a location $7k$ from the front of the domain. Approximately 1.7×10^8 computational cells and 4.5×10^9 particles were used in the computational domain. Figure 6 (bottom) shows the DAC surface mesh on the roughness and flowfield computational cells near the roughness. In the flowfield away from the wall, the computational cells were approximately two to three times larger than the local mean free path. Near the wall, the computational cells were refined to achieve mean free path resolution, and an increased particle density was imposed in these near-wall cells to ensure convergence in the surface quantities.¹⁷ Nearest neighbor collision pairing was used throughout the entire domain to further enhance the computational resolution.

Two DPLR solutions were generated for comparison to the hybrid solution; the first solution employs a no-slip isothermal wall condition at the surface, while the second solution uses a slip wall condition. The DPLR solutions and the DAC hybrid solution have a constant wall temperature of $T_w = 791K$, which is equivalent to the radiative equilibrium wall temperature at the streamwise location of the roughness on a flat plate.

As the boundary layer flow passes over the surface roughness, several interesting flow features could be observed. Figure 7 shows the surface heating on the roughness itself as well as the heating to the surface downstream. A band of relatively strong wall heating originating from the leading edge of the roughness extends many roughness heights downstream. A very weak band of increased surface heating can be observed downstream of the trailing edge as well. The wall heating footprint on the surface surrounding the roughness and downstream may be attributed to the near-wall vortices which are shown in Figure 7 (top) using the Q criterion.²⁶ The collar vortices (the outermost vortex pair (*A*) in Figure 7) form very near the wall in front of the roughness and are relatively weak. The second vortex pair (pair (*B*) in Figure 7) forms over the leading and trailing edge shoulders of the hump, and are relatively stronger. A third vortex pair is evident near the centerline of the roughness in the wake, although only one vortex is detected (vortex (*C*)). This vortex is located further away from the wall compared to the other vortices and is gradually lifted away from the wall downstream. A fourth vortex pair (*D*) is found on the windward side of the roughness, and is seen in the

Table 3. Geometry-dependent non-dimensional flowfield parameters

	$k(r_1 = 20.0\text{mm})$	$k(r_1 = 2.0\text{mm})$
Re_{x_c}	1.78×10^4	1.78×10^4
Re_{δ_T}	5.96×10^2	5.96×10^2
Re_{kk}	1.00×10^2	1.00×10^2
k/δ_T	0.25	0.25
λ_k/k	0.0183	0.0183
λ_w/k	0.0054	0.0054
λ_k/r_1	0.08	0.8
λ_w/r_2	0.0139	0.0204

surface contours as the wisp of increased heating along the leading edge near the wall (Figure 7 (bottom)).

A three-dimensional shock and expansion system forms due to the presence of the roughness, as shown in Figure 8 by the contours of number density. The contours shown represent the flowfield quantities in a constant-z plane at the spanwise center of the domain, and the plane slices through the roughness geometry at $x = 10.45\text{m}$. The shock forms upstream of the leading edge of the roughness in an interaction region where the roll-up of the vortex structures in front of the roughness create an effective displacement of the shock from the actual surface of the roughness. The shock weakens and becomes more oblique along either side of the leading edge. This interaction region is evident in the contours of number density immediately upstream of the roughness, and is also highlighted by the Q-isosurfaces shown previously in Figure 7. Comparison of the general strength and angle of the oblique shock show good agreement between the two DPLR and hybrid DAC solutions.

At this streamwise location on the flat plate, the boundary layer flow upstream of the roughness is generally in (or is very close to) thermal equilibrium. As the flow approaches the roughness however, the flow is processed by the shock and expansion, forming regions of thermal non-equilibrium in the vicinity of the roughness. The extent of thermal non-equilibrium in the flowfield is quantified as the difference between the local translational and vibrational temperatures, $T_{NEQ} = T_{tr} - T_{vib}$. This quantity is shown in a slice at the spanwise center of the domain, $z = 0\text{m}$ in Figure 9. Positive values of T_{NEQ} indicate that the vibrational temperature is lagging the translational temperature, and vice versa for negative values. The shock and expansion regions predicted by DPLR and DAC show similar amounts of vibrational non-equilibrium, but a band of increased vibrational non-equilibrium is observed in the hybrid DAC solution in the shear layer region downstream of the roughness. The maximum vibrational non-equilibrium predicted by DPLR in this shear layer region is approximately 8% of the boundary layer edge temperature, whereas the hybrid DAC solution indicates vibrational non-equilibrium that is approximately 15% of the boundary layer edge temperature. While the difference is modest, it is important to consider the significance of thermal non-equilibrium in this region of the flowfield. When the vibrational temperature departs from equilibrium in a shock, expansion or shear layer, the energy is acquired by (or removed from) the translational and rotational modes until a sufficient number of collisions are achieved to fully thermalize the gas. Before this thermalization however, the gas mixture has a temporary (or local) elevated translational temperature, which affects the local pressure field. Figure 10 shows a planview of the surface pressure contours on and around the roughness from the hybrid DAC solution. The black solid lines show the contour levels from the DPLR slip wall solution, and the black dashed lines show the surface pressure contour levels from the DPLR no-slip wall solution. The windward side of the roughness exhibits a higher pressure as the flow is impeded by the roughness, and the flow expands over the leeward side. The DPLR slip wall and no-slip wall solutions are in good agreement with each other, but show non-negligible differences with the hybrid DAC solution. It is interesting to note that the largest discrepancies in the surface pressure predictions appear to lie beneath the regions of the flow where thermal non-equilibrium is prevalent. This suggests that the local differences in thermal non-equilibrium predicted by the solvers influence the surface pressure distribution, and, moreover, the flowfield pressure itself.

Figures 11 and 12 show the number density contours and streamwise velocity contours at a location approximately $10k$ downstream of the roughness center. The roughness (not shown in the figure) is upstream of this slice and spans $(-0.4\text{m} < z < 0.4\text{m})$. The expanded flow region can be seen in both solutions at

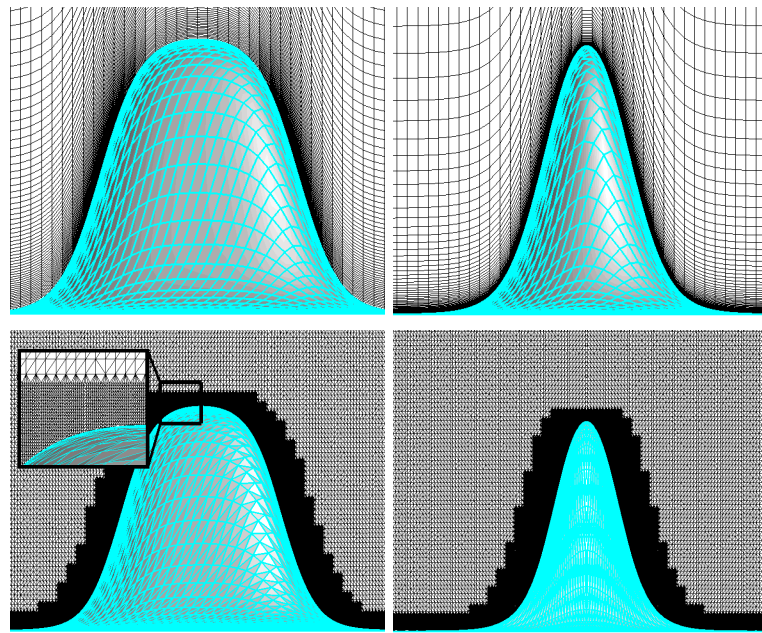


Figure 6. Computational meshes used in flowfield solutions. The upper left and right meshes were used in the DPLR solution, each constructed with approximately 7×10^6 grid points, with wall-normal spacing of 1.0×10^{-5} . The lower left and right meshes were used in the DAC solution, each constructed with approximately 1.7×10^8 computational cells and nearly 5.0×10^9 particles. Near-wall computational cells were refined to enhance resolution at the wall.

this downstream location in the number density contours, and closer to the wall, the wake flow structures are nearly identical between the two flow solvers. The structure in the wake indicates two primary counter-rotating vortices: the first is centered over $z = 0.0m$ and is counter-rotating, while the second is rotating in the clockwise sense centered over $z = 0.3m$. The rotation of the pair drives relatively high-speed flow toward the wall, and lifts low-speed flow away from the wall, as evident in the streamwise velocity contours. Note that more high-speed flow has penetrated toward the wall in the vortex centered over $z = 0.0m$ compared to the weaker vortex centered over $z = 0.3m$.

The surface heating is compared among the DAC hybrid solution and the DPLR slip and no-slip solutions in Figure 13. The region of the surface shown in these figures represents only a small part of the DPLR solution, but shows the full extent of the DAC hybrid domain. The surface heating shown by the contours represent the local surface heat flux normalized by heat flux value on the flat plate at the roughness center x_c , expressed as q_w/q_o . In all cases, the highest heating occurs on the leading edge of the roughness, with bias toward the windward side. The DPLR solution with a no-slip wall condition predicts a peak heating of $q_w/q_o = 9.25$, while the slip-wall condition and DAC hybrid solution predict lower peak heating on the roughness; the peak heating value from the slip-wall condition was 13% lower than the no-slip solution, with $q_w/q_o = 8.05$ and the peak heating predicted by the hybrid DAC solution was 30% lower, with $q_w/q_o = 6.36$. The surface heating along the top of the roughness diminishes toward the trailing edge in all cases examined. Velocity slip was also found to be maximum on the roughness at the leading edge, but the region of maximum slip from the hybrid DAC solution was on the shoulder of the roughness, whereas the slip predicted by the DPLR slip wall model was biased toward the leeward side. The magnitudes of velocity slip predicted by the DPLR slip wall model and the hybrid DAC solution were nearly indistinguishable, with the maximum velocity slip from both solutions being 10% of the boundary layer edge velocity. The details of the velocity slip and surface heating on the roughness shoulder are discussed in the next section.

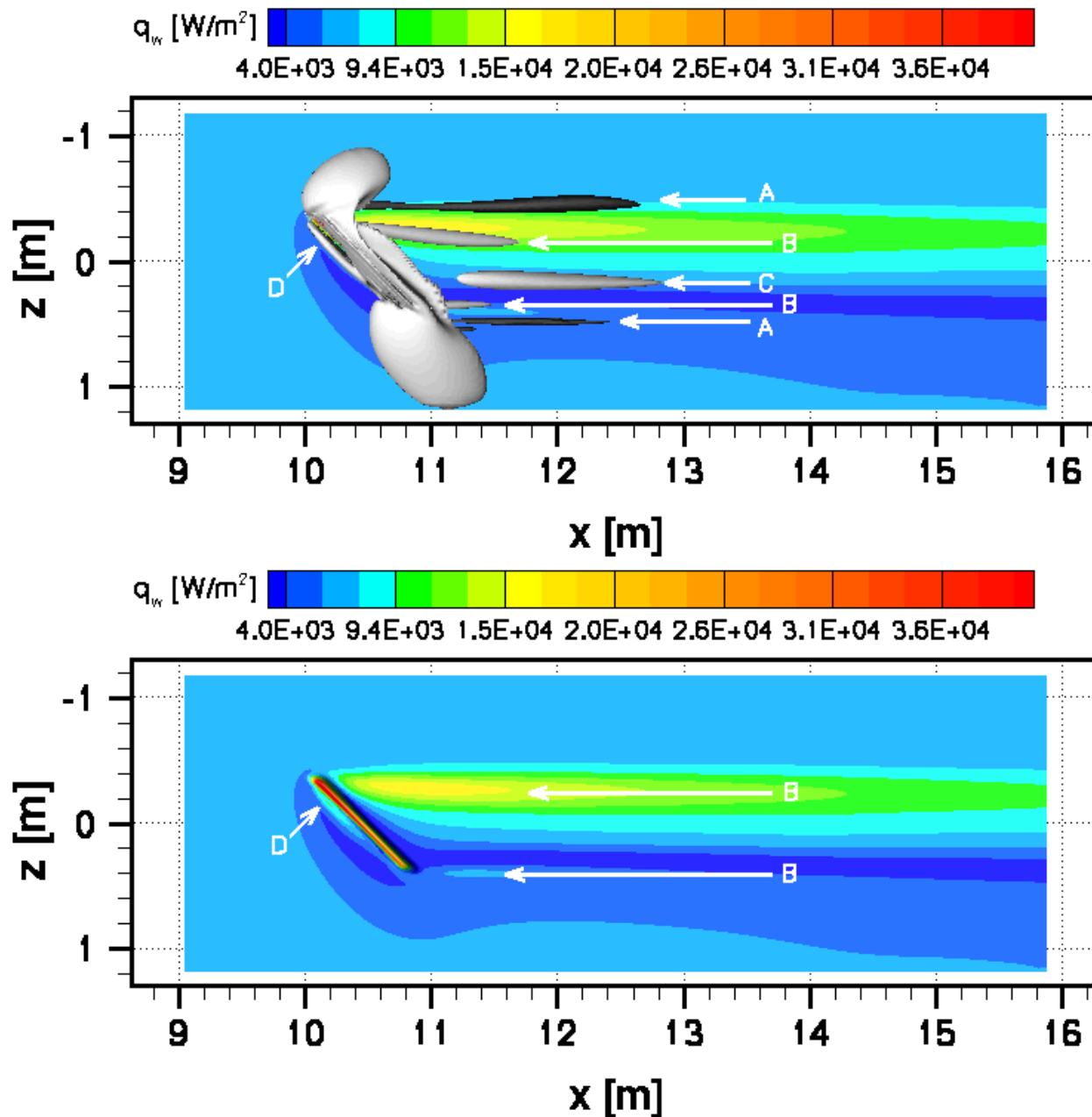


Figure 7. (top) Vortex structures shown by the Q-criterion are overlaid on the surface heat flux contours to elucidate the origin of the heating augmentation in the wake. (bottom) Contours of the surface heating on the roughness and on the surface downstream. Flow is from left to right in all figures.

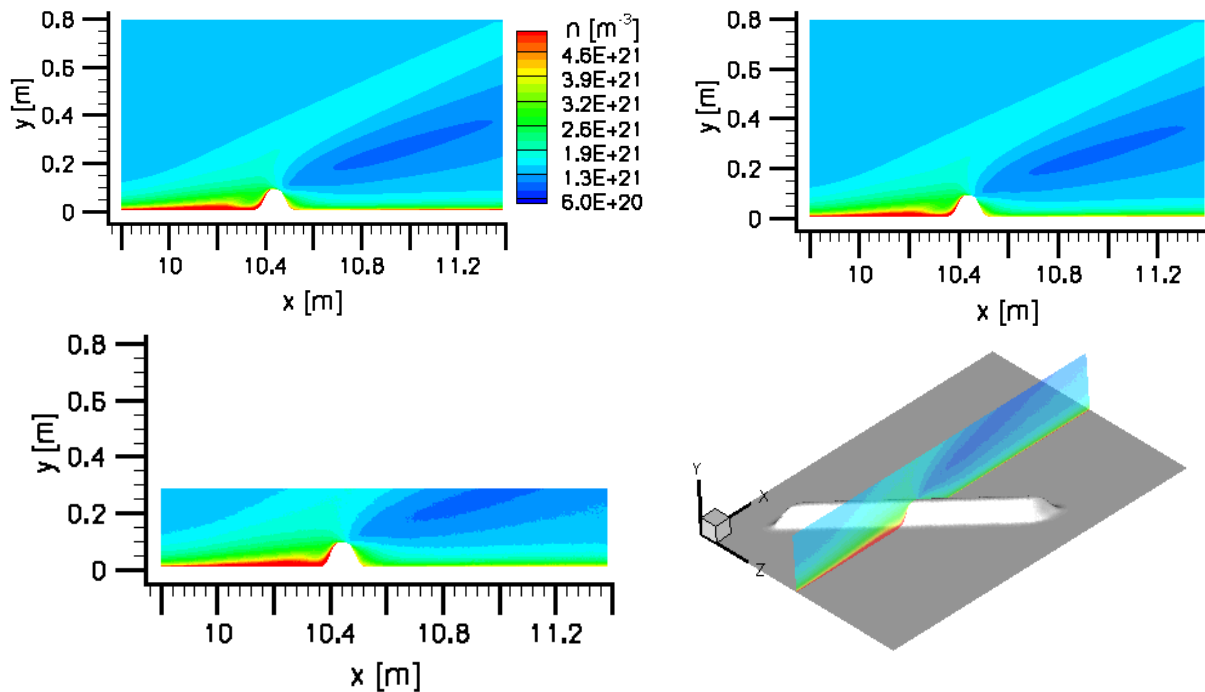


Figure 8. Contours of number density shown in a flowfield slice taken at the spanwise center of the domain (shown in bottom right schematic) for the DPLR no-slip wall condition (upper left), DPLR slip wall condition (upper right) and hybrid DAC (lower left) solutions for the roughness with $r_1 = 20.0\text{mm}$. The slice cuts through the geometry centered over $x = 10.45\text{m}$.

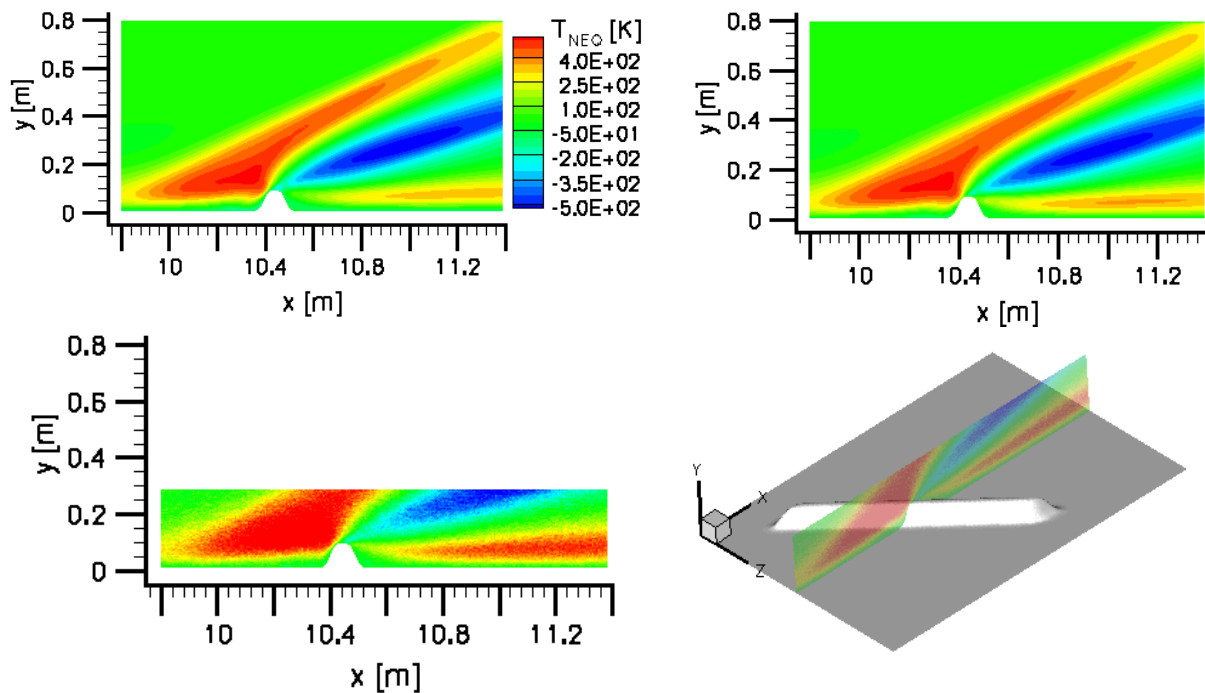


Figure 9. Contours of translational-vibrational non-equilibrium (T_{NEQ}) shown in a flowfield slice taken at the spanwise center of the domain (shown in bottom right schematic) for the DPLR no-slip wall condition (upper left), DPLR slip wall condition (upper right) and hybrid DAC (bottom left) solutions for the roughness with $r_1 = 20.0\text{mm}$. The slice cuts through the geometry centered over $x = 10.45\text{m}$.

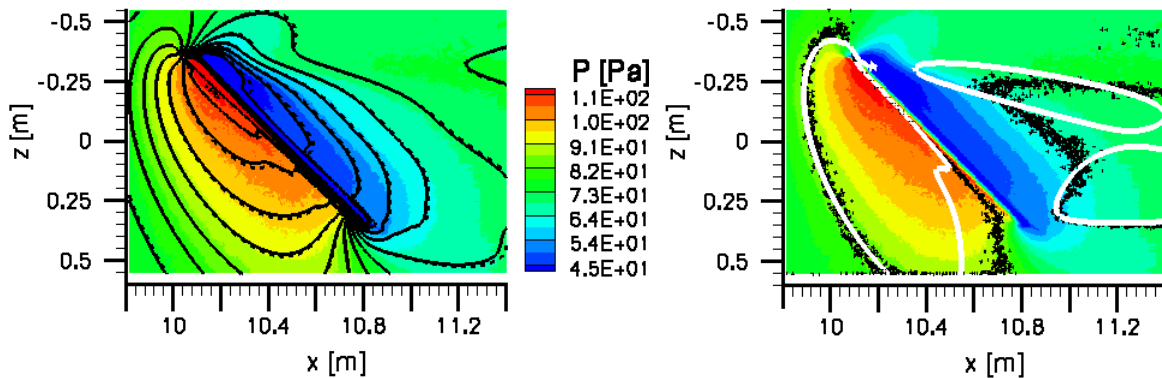


Figure 10. (Left) Planview of the surface in the region of the roughness. Contours show the surface pressure from the hybrid DAC solution, solid black isocontour lines represent the contours from the DPLR slip solution, and dashed black lines represent the DPLR no-slip solution. Flow is from left to right. (Right) Planview of the surface in the region of the roughness. Contours again show the surface pressure predicted by the hybrid DAC solution. Isocontours are shown to highlight the regions of translational-vibrational non-equilibrium in a constant- y slice taken at the height of the roughness. The isocontours show regions of $T_{NEQ} = 350K$, which was 75% of the maximum thermal non-equilibrium observed in the wake. White lines represent the DPLR slip solution, and black lines represent the hybrid DAC solution.

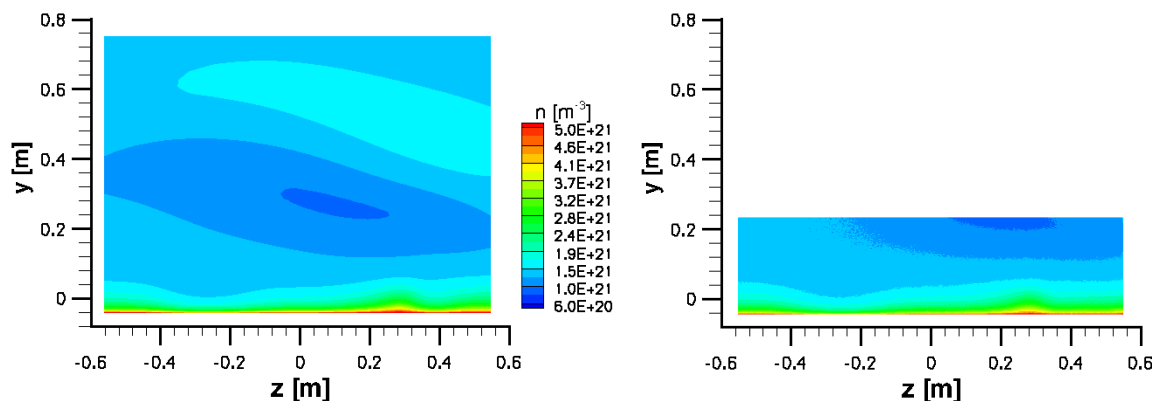


Figure 11. Contours of number density shown in a flowfield slice taken at a location $10k$ downstream of the roughness center for the case $r_1 = 20.0mm$. Contours represent the DPLR slip wall condition (left), hybrid DAC (right) solutions. The hybrid solution shows the full extent of the computational domain, and flow is into the page.

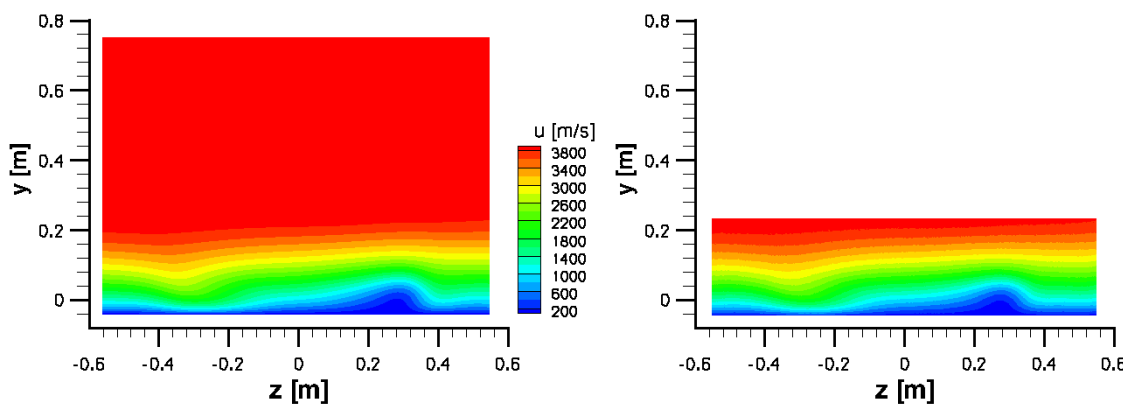


Figure 12. Contours of streamwise velocity shown in a flowfield slice taken at a location $10k$ downstream of the roughness center for the case $r_1 = 20.0\text{mm}$. Contours represent the DPLR slip wall condition (left), hybrid DAC (right) solutions. The hybrid solution shows the full extent of the computational domain, and flow is into the page.

C. DPLR and Hybrid Solutions – Case 2: $r_1 = 2.0\text{mm}$

The second set of cases examine the flowfield solution from the roughness geometry with a radius of curvature $r_1 = 2.0\text{mm}$. The Knudsen number based on the radius of curvature r_1 ($Kn = \lambda/r_1$) is quite large when λ is computed from the mean free path in the undisturbed boundary layer flow. However, it is important to note that the boundary layer flow approaching the roughness is first processed by the roughness-induced oblique shock, and so the actual local mean free path at the top of the roughness in this case is approximately 0.4mm . The radius of curvature is thus five times the local mean free path, based on the hard sphere approximation.

In Figure 14, the number density contours are shown in a spanwise-centered slice at $z = 0$ from the DPLR no-slip solution (upper left), the DPLR slip wall solution (upper right) and the hybrid DAC solution (lower left). Although the radius of curvature at the wall is smaller in this case than in the previous geometry, the shock/boundary layer interaction region upstream of the roughness develops in much the same manner as in the previous case. The shock and expansion regions show good agreement among the three solutions. The translation-vibrational thermal nonequilibrium is shown in Figure 15, and the hybrid DAC solution again predicts stronger thermal non-equilibrium in the shock, expansion and shear layer regions. It is interesting to note that the DPLR slip wall solution (Figure 15, upper right) shows slightly higher thermal non-equilibrium in the shear layer relative to the no-slip DPLR solution. This suggests that the thermal non-equilibrium in the shear layer may be driven in part by the wall condition at the top of the roughness.

The surface heating to the roughness and the surrounding area is shown in Figure 17 for the no-slip wall and slip wall DPLR solutions and the hybrid DAC solution. The peak heating to the roughness is substantially higher due to the small radius of curvature of this roughness, $r_1 = 2.0\text{mm}$ compared to the previous case. The DPLR no-slip solution predicts a peak surface heating of $q_w/q_o = 18.06$, while the slip wall condition peak heating is 25% lower, with a value of $q_w/q_o = 13.48$. The hybrid DAC solution predicts a surface heating that is nearly 50% lower with a value $q_w/q_o = 9.92$. The most substantial heating to the surface of the roughness occurs on the windward side of the roughness, as shown in the accompanying figures which show a close-up view of the heating at the leading edge. The velocity slip is found to be maximum on the shoulder and leeward side of the roughness, shown in detail in Figure 16 for the slip wall DPLR solution and the hybrid DAC solution. The white iso-contour line highlights the region of velocity slip at the surface of the roughness where the slip value exceeds $0.10u_e$. This region is relatively rarefied as the flow undergoes expansion as it passes over the shoulder of the bump. The region of maximum velocity slip was found to be different between the DPLR and DAC solutions, as shown by the white isoline and the grey shaded isosurface on the shoulder of the bump. The magnitude of the maximum velocity slip predicted by the two methods was approximately 500m/s , or 13% of the boundary layer edge velocity, but the acreage of the velocity slip on the top of the roughness was more expansive than the hybrid solution, which predicts a more localized region of high velocity slip. This did not have a noticeable affect on the surface properties

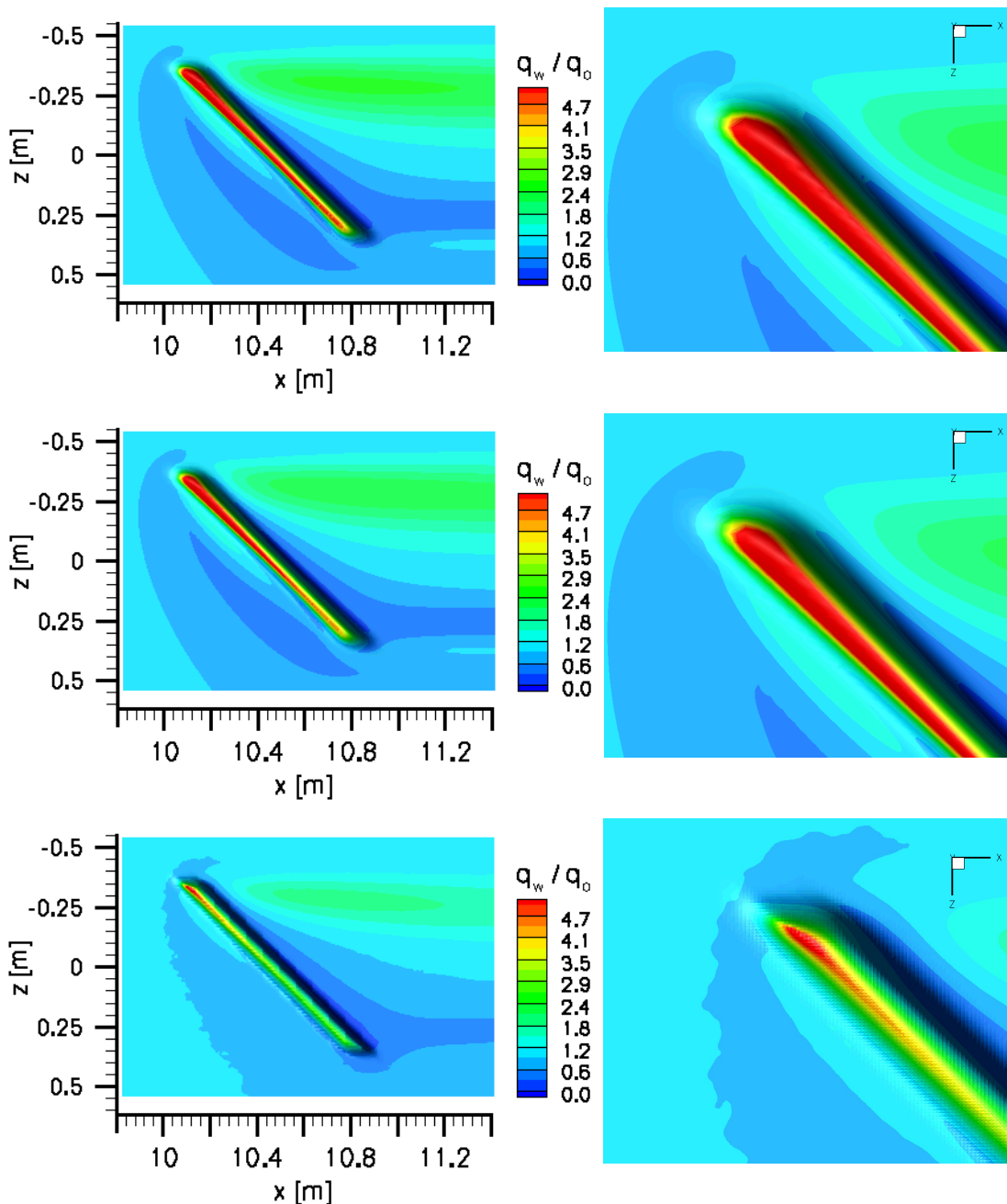


Figure 13. Contours of surface heat flux in the region near the roughness as predicted by the DPLR *no-slip* solution (top), the DPLR *slip* solution (middle) and the hybrid DAC solution (bottom) for the case $r_1 = 20.0\text{mm}$. Contours represent the local surface heat flux normalized by the flat plate heat flux value at the location of the roughness center. The surface heating near the leading edge is shown enlarged for each case in the figures on the right. Note that the general heating footprint near the roughness is very similar among the cases, but the peak surface heating to the roughness is largest in the DPLR no-slip solution ($q_w/q_o = 9.25$), while the DPLR slip wall solution and DAC hybrid solutions predict a peak heating of $q_w/q_o = 8.05$ and $q_w/q_o = 6.36$, respectively.

or the local flowfield. A summary of the maximum velocity slip and peak surface heating obtained for the roughness geometries examined is provided in Table 4. The slip velocities are normalized by the boundary layer edge velocity, and the local surface heat fluxes q_w are normalized by the wall heating of an undisturbed boundary layer flow over a flat plate at the location of the roughness, q_o .

Table 4. Predicted surface roughness properties

$r_1 = 20.0\text{mm}$	DPLR no-slip wall	DPLR slip wall	DAC hybrid
V_{slip}/u_e	—	0.10	0.10
q_w/q_o	9.25	8.05	6.36
$r_1 = 2.0\text{mm}$			
V_{slip}/u_e	—	0.13	0.13
q_w/q_o	18.06	13.48	9.92

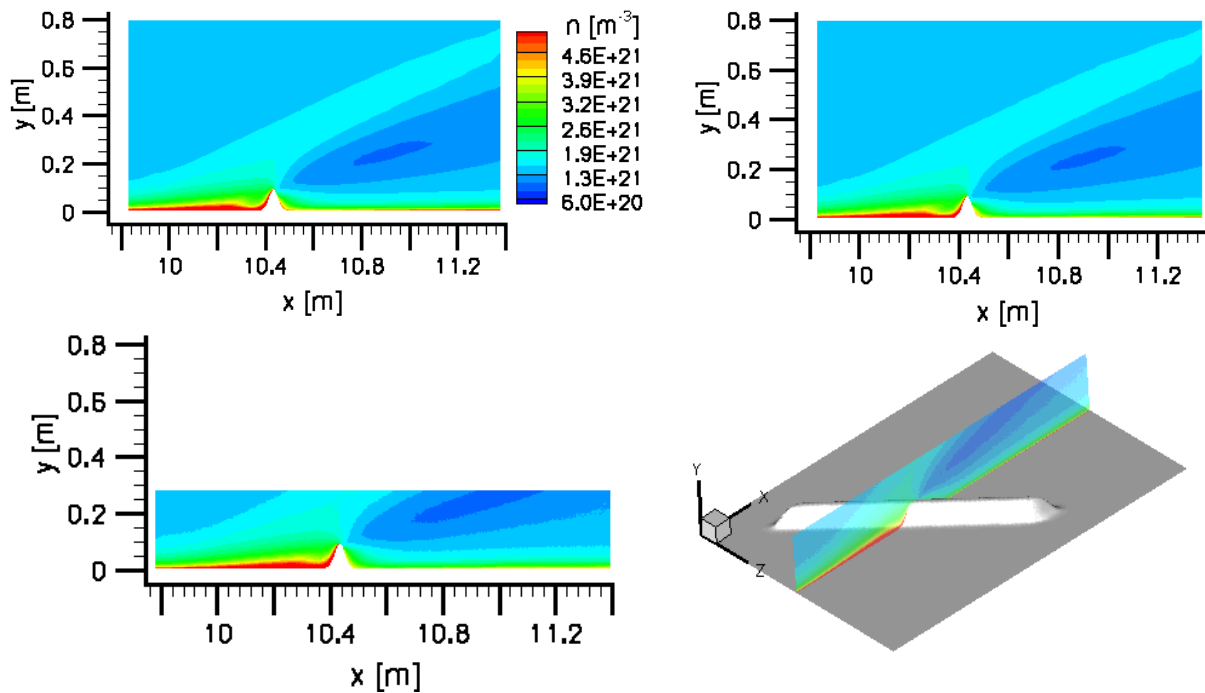


Figure 14. Contours of number density shown in a flowfield slice taken at the spanwise center of the domain (shown in the bottom right schematic) for the DPLR no-slip wall condition (upper left), DPLR slip wall condition (upper right) and hybrid DAC (bottom left) solutions. The slice cuts through the geometry centered over $x = 10.45\text{m}$, and the roughness shown corresponds to the case $r_1 = 2.0\text{mm}$.

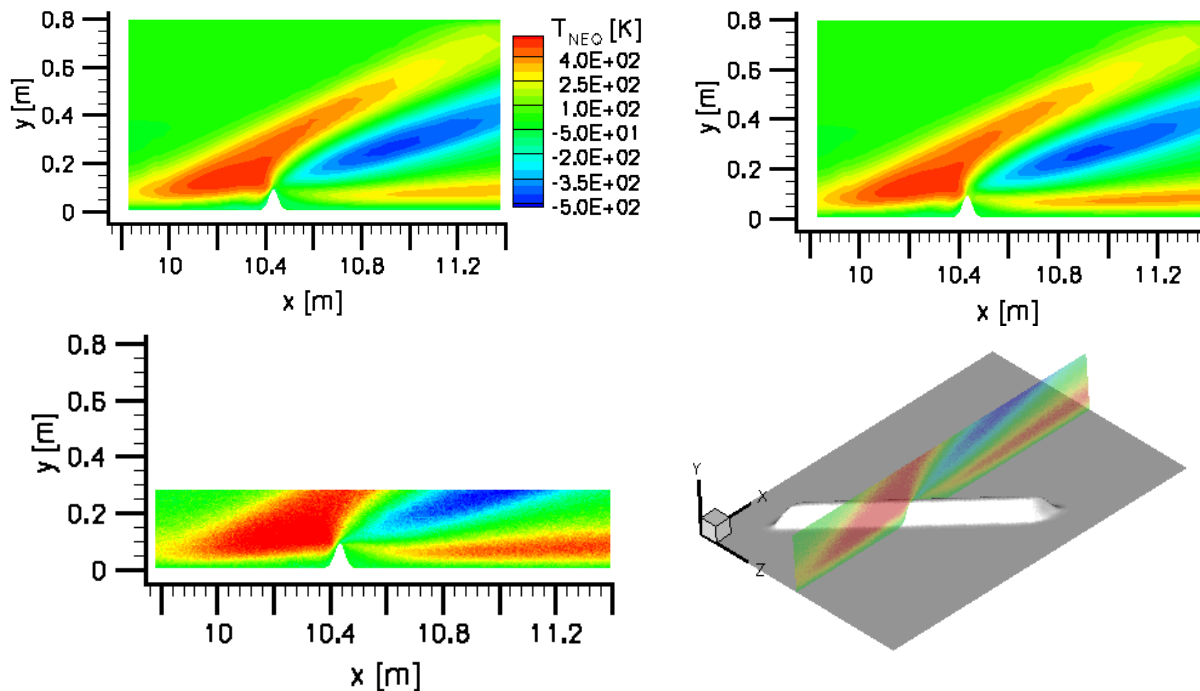


Figure 15. Contours of translational-vibrational non-equilibrium shown in a flowfield slice taken at the spanwise center of the domain (shown in bottom right schematic) for the DPLR no-slip wall condition (upper left), DPLR slip wall condition (upper right) and hybrid DAC (bottom left) solutions. The slice cuts through the geometry centered over $x = 10.45\text{m}$, and the roughness shown corresponds to the case $r_1 = 2.0\text{mm}$

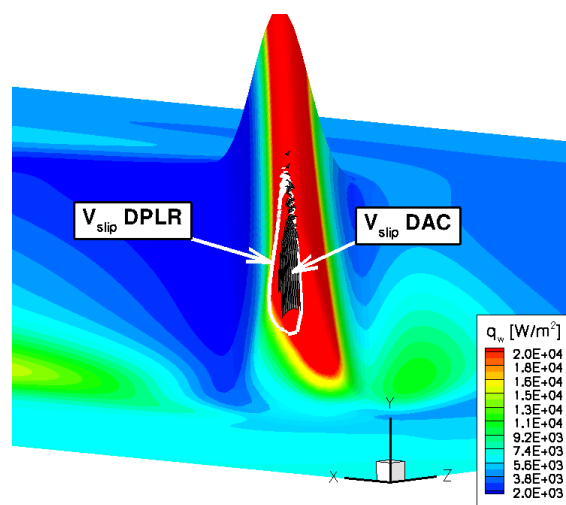


Figure 16. Contours of surface heat flux [W/m^2] in the region near the $r_1 = 2.0\text{mm}$ roughness. The view shows the detail of the leading edge, and flow is from *right to left*. The white isocontour represents 10% slip velocity at the surface of the roughness predicted by the DPLR slip wall solution, and the grey shaded isosurface represents 10% slip velocity from the hybrid DAC solution. In all solutions examined, the peak surface heating occurred on the top of the roughness near the leading edge, and the maximum heating was biased toward the windward side of the geometry. In contrast, the peak velocity slip was biased toward the leeward side of the geometry.

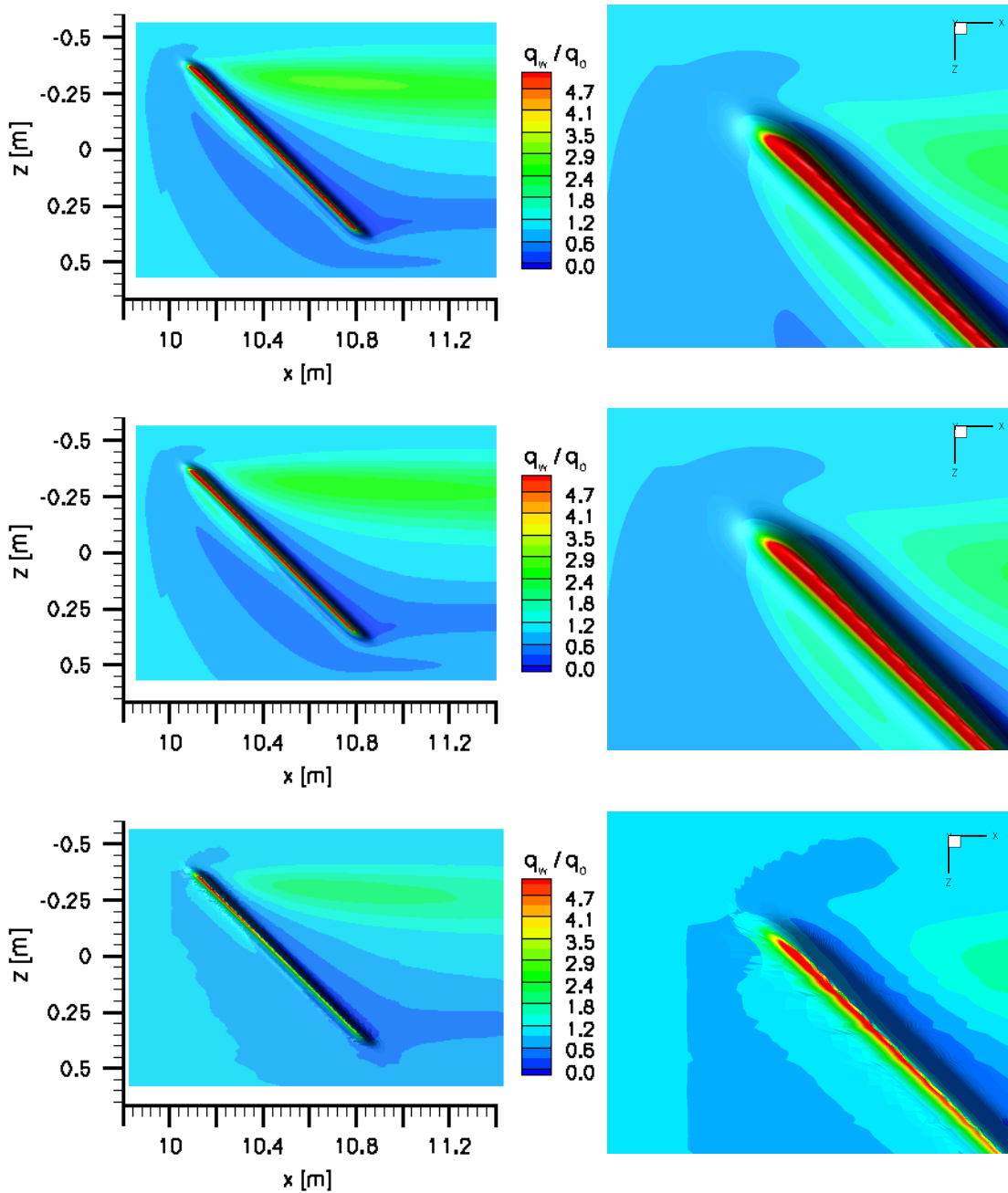


Figure 17. Contours of surface heat flux in the region near the roughness as predicted by the DPLR *no-slip* solution (top), the DPLR *slip* solution (middle) and the hybrid DAC solution (bottom) for the case $r_1 = 2.0\text{mm}$. Contours represent the quantity q_w/q_o , which is the local surface heat flux normalized by the heat flux at the location of the roughness center on a flat plate. The surface heating near the leading edge is shown enlarged for each case in the figures on the right. Note that the general heating footprint near the roughness is very similar among the cases, but the peak surface heating to the roughness is largest in the DPLR no-slip solution ($q_w/q_o = 18.06$), while the DPLR slip wall solution and the DAC hybrid solution both predict a lower peak heating of $q_w/q_o = 13.48$ and $q_w/q_o = 9.92$, respectively.

IV. Conclusions

The effects of rarefaction on hypersonic boundary layer flow over various discrete surface roughness configurations were examined in a parametric study of $M_\infty = 3.0$ flow over discrete roughness on a flat plate. The roughness height was held fixed and was chosen such that the local Knudsen number ($Kn = \lambda/k$) in the region of the roughness was $O(10^{-2})$. Two radii of curvature prescribing the shape of the top of the roughness were examined, and hybrid DAC solutions were generated and compared to the DPLR solutions generated with slip and no-slip wall conditions.

The vibrational non-equilibrium observed in the shock, expansion and shear layer regions surrounding the roughness was found to impact the pressure at the surface. In these regions of thermal non-equilibrium, the vibrational temperature lags the translational temperature in the expanded flow region downstream of the roughness, and it leads the translational temperature in the oblique shock as well as in the shear layer. A finite number of inelastic collisions are required to thermalize the vibrational mode, until an equilibrium energy state has been achieved by the mixture. During this relaxation process, the translational temperature relaxes toward the equilibrium state, producing a local gradient in translational temperature due to thermal equilibration. Since the DPLR and hybrid DAC solutions exhibited different amounts of vibrational non-equilibrium in the shock, expansion and shear layer generated by the roughness, it is suggested that this local temperature gradient gives rise to the difference in the surface pressure observed in the solutions. Although the vibrational relaxation models used in the present study have demonstrated good agreement in vibrational relaxation in a five-species air heat bath,²⁵ it is possible that the relaxation rates may behave differently in a highly sheared boundary layer, and so this approach should be validated for extension to boundary layer flow.

The DPLR slip model predicts higher velocity slip near the expansion region at the surface of the roughness. The total heat flux on the surface of the protuberance was also examined. It was found that the hybrid DAC solution predicts a heating augmentation to the roughness that is 20–30% below the DPLR slip wall solution, and 30–50% below the DPLR no-slip wall solution for the roughness configurations examined.

V. Acknowledgements

This work was funded by the NASA NRA under contract agreement NNX08AB27A with monitor Dr. Deepak Bose. Computational resources and technical support were provided by TACC at the University of Texas at Austin.

References

- ¹Anderson, J. D., *Hypersonic and High Temperature Gas Dynamics*, AIAA, Inc., Reston, VA, 2000.
- ²Reshotko, E. and Tumin, A., "Role of transient growth in roughness-induced transition," *AIAA Journal Vol. 42 No. 4*, April 2004.
- ³Schneider, S. P., "Effects of Roughness on Hypersonic Boundary-Layer Transition," *45th AIAA Aerospace Sciences Meeting and Exhibit*, January 2007, Reno, NV 2007, pp. AIAA 2007-0305.
- ⁴Campbell C. H., Garske M. T., K. J. and A., B. S., "Orbiter Entry Boundary Layer Flight Testing," *46th AIAA Aerospace Sciences Meeting and Exhibit*, 7-10 January 2008, Reno, Nevada 2008, pp. AIAA 2008-0635.
- ⁵Bird, G., *Molecular Gas Dynamics and the Direct Simulation of Gas Flows*, Oxford University Press, Oxford, 1994.
- ⁶Danehy P. M., Garcia A. P., B. S. D. A. A. B. S. A. W. I. J. A. A. D. W., "Fluorescence visualization of hypersonic flow past triangular and rectangular boundary-layer trips," *45th AIAA Aerospace Sciences Meeting and Exhibit*, January 2007, Reno, NV 2007, pp. AIAA 2007-0536.
- ⁷Chang, C. L. and Choudhari, M. M., "Hypersonic Viscous Flow over Large Roughness Elements," *47th AIAA Aerospace Sciences Meeting and Exhibit*, January 2009, Orlando, FL 2009, pp. AIAA 2009-0173.
- ⁸Rizzetta, D. P. and Visbal, M. R., "Direct Numerical Simulations of Flow Past an Array of Distributed Roughness Elements," *36th AIAA Fluid Dynamics Conference and Exhibit*, June 2006, San Francisco, CA 2006, pp. AIAA 2006-3527.
- ⁹Stephani, K. A. and Goldstein, D. B., "DNS Study of Transient Disturbance Growth and Bypass Transition due to Realistic Roughness," *47th AIAA Aerospace Sciences Meeting and Exhibit*, January 2009, Orlando, FL 2009, pp. AIAA 2009-0585.
- ¹⁰Glass, C. E. and Horvath, T. J., "Comparison of a 3D CFD-DSMC Solution Methodology With a Wind Tunnel Experiment," *NASA/TM-2002-211777*, 2002.
- ¹¹Roveda R., Goldstein, D. B. and Varghese, P. L., "Hybrid Euler/DSMC approach for continuum/rarefied flows," *Journal of Spacecraft and Rockets*, Vol. 35, No. 4, May-June 1998.
- ¹²Stewart, D. A., "Surface Catalysis and Characterization of Proposed Candidate TPS for Access-to-Space Vehicles," *NASA TM 112206*, July 1997.

- ¹³LeBeau, G. J. and Lumpkin, F. E. I., "Application highlights of the DSMC Analysis Code (DAC) software for simulating rarefied flows," *Computer Methods in Applied Mechanics and Engineering*, Vol. 191, Issues 6-7 pp. 595-609, December 2001.
- ¹⁴Wright M. J., Candler G. V., B. D., "Data-Parallel Line Relaxation Method for the Navier-Stokes Equations," *AIAA Journal*, Vol. 36, No. 9, September 1998.
- ¹⁵NASA, "STS-119 Infrared image," <http://spaceflightnow.com/shuttle/sts119/090329blt/>, 2009.
- ¹⁶Garcia, A. and Wagner, W., "Generation of the Maxwellian Inflow Distribution," *Journal of Computational Physics* 217 693-708, 2006.
- ¹⁷Stephani, K. A. Goldstein, D. B. and Varghese, P., "Development of a Hybrid DSMC/Navier-Stokes Solver with Application to the STS-119 Boundary Layer Transition Flight Experiments," *49th AIAA Aerospace Sciences Meeting and Exhibit*, January 2011, Orlando, FL 2011, p. to appear in proceedings.
- ¹⁸Garcia, A. and Alder, W., "Generation of the Chapman-Enskog Distribution," *Journal of Computational Physics* 140 66, 1998.
- ¹⁹Gupta R., Yos J., T. R., "A Review of Reaction Rates and Thermodynamics and Transport Properties for the 11-Species Air Model for Chemical and Thermal Nonequilibrium calculations to 30000K," *NASA TM 101528*, February 1989.
- ²⁰Hirschfelder J., C. C. and R., B., *Molecular Theory of Gases and Liquids*, John Wiley & Sons Inc, New York, 1967.
- ²¹Millikan, R. C. and White, D. R., "Systematics of Vibrational Relaxation," *Journal of Chemical Physics*, Vol. 39, No. 12, pp 3209-3213, 1963.
- ²²Park, C., "Review of Chemical-Kinetic Problems of Future NASA Missions, I: Earth Entries," *Journal of Thermophysics and Heat Transfer*, Vol. 7, No. 3, 1993.
- ²³Gimelshein, N. E., G. S. F. and Levin, D. A., "Vibrational relaxation rates in the direct simulation Monte Carlo method," *Physics of Fluids*, Vol. 14, No. 12, 2002.
- ²⁴Deschenes, T. R., H. T. D. B. I. D. and Schwartzentruber, T. E., "Analysis of internal energy transfer within a modular particle-continuum method," *AIAA Paper No. 2009-1216*, 2009.
- ²⁵Holman, T. D. and Boyd, I. D., "Effects of Continuum Breakdown on hypersonic aerothermodynamics for reacting flow," *Physics of Fluids*, Vol. 23, 2011.
- ²⁶Green, M. A., R. C. W. and Haller, G., "Detection of Lagrangian coherent structures in three-dimensional turbulence," *Journal of Fluid Mechanics*, Vol. 572, pp. 111-120, 2007.